Electrochemistry of single nanobubbles. Estimating the critical size of bubble-forming nuclei for gas-evolving electrode reactions

Sean R. German,[ab] Martin A. Edwards,[a] Qianjin Chen,[a] Yuwen Liu,[a] Long Luo[c] and Henry S. White*[a]

In this article, we address the fundamental question: "What is the critical size of a single cluster of gas molecules that grows and becomes a stable (or continuously growing) gas bubble during gas evolving reactions?" Electrochemical reactions that produce dissolved gas molecules are ubiquitous in electrochemical technologies, *e.g.*, water electrolysis, photoelectrochemistry, chlorine production, corrosion, and often lead to the formation of gaseous bubbles. Herein, we demonstrate that electrochemical measurements of the dissolved gas concentration, at the instant prior to nucleation of an individual nanobubble of H_2, N_2, or O_2 at a Pt nanodisk electrode, can be analyzed using classical thermodynamic relationships (Henry's law and the Young–Laplace equation – including non-ideal corrections) to provide an estimate of the size of the gas bubble nucleus that grows into a stable bubble. We further demonstrate that this critical nucleus size is independent of the radius of the Pt nanodisk employed (<100 nm radius), and weakly dependent on the nature of the gas. For example, the measured critical surface concentration of H_2 of $\sim$0.23 M at the instant of bubble formation corresponds to a critical H_2 nucleus that has a radius of $\sim$3.6 nm, an internal pressure of $\sim$350 atm, and contains $\sim$1700 H_2 molecules. The data are consistent with stochastic fluctuations in the density of dissolved gas, at or near the Pt/solution interface, controlling the rate of bubble nucleation. We discuss the growth of the nucleus as a diffusion-limited process and how that process is affected by proximity to an electrode producing $\sim$10^{11} gas molecules per second. Our study demonstrates the advantages of studying a single-entity, *i.e.*, an individual nanobubble, in understanding and quantifying complex physicochemical phenomena.

[a]*University of Utah, Department of Chemistry, 315 S 1400 E Salt Lake City, Utah 84112, USA. E-mail: white@chem.utah.edu*

[b]*Revalesio Corporation, 1200 East D Street, Tacoma, Washington 98421, USA*

[c]*The University of Texas at Austin, Department of Chemistry and the Texas Materials Institute, 105 East 24th Street, Stop A5300, Austin, Texas 78712, USA*

Introduction

The spontaneous phase transformation required to initiate bubble formation is a highly activated process requiring extreme conditions. Classical nucleation theory (CNT) describes the activation barrier to create a bubble nucleus in terms of the cohesive force of the liquid, while assuming a critical nucleus is large enough that it can be described by bulk thermodynamics.[1–4] CNT applies equally to single component systems, where a vapor bubble is generated by single component boiling,[5,6] as well as binary mixtures, where a dissolved gas phase separates into a bubble;[7–10] these two systems differ predominantly in their growth/dissolution dynamics. Vapor bubbles in single component systems are at all instances surrounded by their comprising material and are often violent in their dynamics, such as with cavitation.[5] Diffusional gradients control the growth of bubbles formed from dissolved gas. In this work, we report on nucleation of individual gas bubbles from a supersaturated binary mixture engendered by electrogeneration of dissolved gas at Pt nanodisk electrodes.

The free energy of formation of a gas bubble nucleus in solution, ΔG_{tot}, is the sum of the energy cost of creating the new interface and that gained through liberation of dissolved gas into the bubble volume. Fig. 1 (top) schematically presents the classic description of ΔG_{tot} as a function of the bubble's radius, r_{nb}. The free energy attributable to the gas/solution interface, $\Delta G_{surf} = 4\pi\gamma r_{nb}^2$ (dashed line, where γ is surface energy of the gas/solution interface), is proportional to the area of the bubble's interface. The bulk component term, ΔG_{bulk}, (dotted line, $(4\pi/3)\Delta G_V r_{nb}^3$) is proportional to the volume of the bubble and ΔG_V, the energy difference between the dissolved and gaseous state of the molecules in that volume. ΔG_{tot} is the sum of these two components,

$$\Delta G_{tot} = 4\pi\gamma r_{nb}^2 + (4\pi/3)\Delta G_V r_{nb}^3 \tag{1}$$

Eqn (1) indicates that ΔG_{tot} initially increases as a function of r_{nb} before reaching a maximum, E_a, at a critical radius, r_{crit}. The implication of this free energy maximum is that a bubble of radius greater than r_{crit} is energetically favored to continue to grow, whereas bubbles with radii less than r_{crit} are inclined to shrink. However, since bubbles of critical size necessarily arise from the growth of sub-critical nuclei, their formation relies upon relatively improbable fluctuations along the free energy barrier.

A bubble of critical radius is both in mechanical and chemical equilibrium with the dissolved gas. The Young–Laplace equation (eqn (2)) describes the pressure difference across the gas/solution interface, $\Delta P_{Y-L} = P_{internal} - P_{ambient}$, where $P_{internal}$ and $P_{ambient}$ are the total pressure within the bubble and the ambient pressure, respectively. For a bubble of radius r_{crit}

$$\Delta P_{Y-L} = 2\gamma/r_{crit}. \tag{2}$$

Large positive values of ΔP_{Y-L} tend to drive gas molecules out of sub-critical bubbles into the solution, resulting in bubble shrinkage. The bubble's internal hydrostatic pressure ($\Delta P_{Y-L} + P_{ambient}$) can be countered when the partial pressure of the dissolved gas, P_{gas}, is equal to the bubble's internal pressure. For any

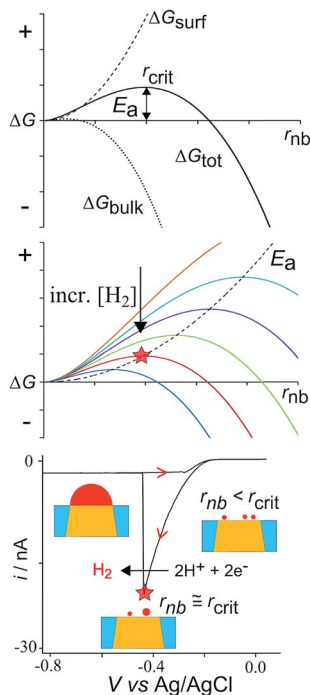Fig. 1 (Top) Plot of total free energy of formation of a gas bubble nucleus, $\Delta G_{tot} = \Delta G_{surf} + \Delta G_{bulk}$, vs. the radius of the nanobubble, r_{nb}. The maximum in ΔG_{tot} corresponds to the critical nanobubble radius, r_{crit}, with an activation energy barrier of E_a. For a bubble nucleus of radius greater than r_{crit}, the continued growth of the nucleus into a stable bubble is energetically favorable. (Middle) Plots of ΔG_{tot} vs. r_{nb} at different concentrations of dissolved H_2 (i.e. different supersaturations). Lower values of $[H_2]$ are associated with higher values of E_a, (indicated by the dashed line), reducing the probability of bubble formation. Increasing $[H_2]$ decreases the activation energy such that thermal fluctuations may nucleate a bubble of critical radius, as depicted by the red star for an arbitrary H_2 concentration. (Bottom) Cyclic voltammogram for H^+ reduction in 0.5 M H_2SO_4 at a 33 nm radius Pt nanodisk electrode (500 mV s^{-1}). The peak (red star) corresponds to a phase change as a nucleus grows into a stable nanobubble covering the electrode. Inlaid schematics show the spontaneous formation of nuclei near the surface of the electrode. At a sufficiently high rate of H_2 electrogeneration and, thus, supersaturation at the electrode/electrolyte interface, a nucleus of critical size may exist, which grows into a bubble covering the electrode. Note: while the schematic shows nucleation as a homogeneous process occurring just above the electrode, we also consider the possibility of heterogeneous nucleation on the electrode surface (see Results and discussion).

specific supersaturation of dissolved gas, $P_{gas} - P_{ambient}$, there is a corresponding E_a required for formation of a continuously growing bubble. As shown in the middle plot of Fig. 1, a critical bubble size is associated uniquely with a specific E_a and supersaturation. As qualitatively illustrated in this figure for H_2 bubble formation, the values of E_a at low supersaturations are sufficiently large such that nuclei are unlikely to reach r_{crit} and grow into stable bubbles. Conversely, large supersaturations of H_2 serve to reduce r_{crit} such that thermal fluctuations of the magnitude of E_a may occur at an appreciable rate.

We recently reported on the formation of single bubbles of H_2, N_2, and O_2 at the surface of Pt nanoelectrodes that are created by electrogeneration of large gas

supersaturations at the electrode/electrolyte interface.[11–15] The lower frame of Fig. 1 shows an example cyclic voltammogram for the formation of a single H_2 bubble. In this experiment, H^+ reduction at a 33 nm radius Pt nanoelectrode in 0.5 M H_2SO_4 is used to drive H_2 production. On the initial sweep of the i–E curve, the current for H_2 electrogeneration increases when the electrode potential, E, is scanned to potentials negative of the formal potential for H^+ reduction $\left(E^0_{H^+/H_2} = -0.23 \text{ V } vs.\text{Ag/AgCl}\right)$. As the potential is scanned to more negative values, the current and rate of H_2 electrogeneration continue to increase nearly exponentially until there is an abrupt drop in the current to a non-zero residual current that is nearly independent of E. The abrupt drop defines the peak current, i^p_{nb}, that coincides with the formation of a stable nanobubble on the surface of the electrode.[12] The bubble, which covers the electrode surface, significantly diminishes the rate of H^+ reduction at the electrode, the latter occurring along the circumference of the bubble at the Pt/gas/electrolyte interface.[11] In this specific voltammogram, the formation of a single bubble occurs at $\sim$−0.4 V, as indicated by the sudden drop in current magnitude from i^p_{nb} $\sim$20 nA to $\sim$3 nA. The bubble is only stable as long as the potential is held sufficiently negative of $\sim$−0.3 V, such that the constant production of H_2 at the electrode circumference replenishes the H_2 that dissolves from the bubble into the solution. As the potential is swept back towards positive potentials, the current for H^+ reduction decays and the bubble rapidly dissolves.[15] Note, throughout this work, our analysis does not require knowledge of the precise mechanism of the gas evolving electrode reactions, only that such reactions produce gas as described by their stoichiometric reactions, $e.g.$, $2H^+ + 2e^- \rightarrow H_2$.

At the foot of the voltammetric wave, the rate of H_2 generation is low, and thus the amount of dissolved H_2 is also correspondingly low. Based on the above description, we expect that the transient H_2 bubble nuclei, schematically shown in the insets of Fig. 1, are smaller than the corresponding r_{crit}, and thus are unstable and dissolve rapidly. As the current is swept to more negative potentials, the concentration ($i.e.$, supersaturation) of dissolved H_2 in the vicinity of the electrode increases and r_{crit} decreases until the probability of a bubble nucleus of radius approaching or exceeding r_{crit} becomes sufficiently large. At this electrode potential, continued growth of a nucleus leading to a stable bubble is thermodynamically favorable. This critical point coincides with the red star on each of the graphs. While the thermodynamics suggest that the bubble will continue to grow ad $infinitum$, its growth is self-limited at the Pt disk edges, which, as noted above, acts as the source of H_2 for its growth.[11] A stable bubble is established in a dynamic steady state when the rate of H_2 dissolution and electrogeneration are equal.

Herein, we show that the value of i^p_{nb}, recorded at the instant prior to formation of a single bubble, is proportional to the electrode size, with a constant of proportionality that depends on the identity of the gas. Our voltammetric results indicate a sharp potential-dependent threshold in nucleation rates, from immeasurably slow to extremely fast. We demonstrate that the peak current corresponds to critical supersaturations for H_2, N_2, and O_2, above which a stable phase transformation immediately proceeds. The critical supersaturation is a direct measure of the chemical potential of gas within the critical bubble nucleus, allowing calculation of the critical nucleus pressure and radius, as well as the number of constituent gas molecules contained within the nucleus.

Results and discussion

Fig. 2 shows typical voltammograms for electrochemical reactions at Pt nano-electrodes that correspond to the formation of stable individual nanobubbles of H_2, N_2, and O_2. Each voltammogram displays a similar shape to that for H_2 nanobubble formation shown in Fig. 1; however, the values of potentials and currents are different for the different gases. In each case we expect the bubble to form from a critically sized nucleus, although the critical radius for each gas will differ due to the distinct chemical properties of the gases. The peak current i_{nb}^p just prior to bubble formation is labeled on each voltammogram. In all cases, i_{nb}^p is reproducible between cycles and is nearly independent of the scan rate up to ~ 10 V s^{-1}.

The reproducibility of i_{nb}^p and insensitivity to scan rate suggests a very sharp threshold in the electrode potential over which the probability of a nucleus having radius greater than r_{crit} changes from essentially zero to unity, and bubble formation immediately proceeds. If the electrode potential threshold was more gradual, one would expect significant variability in i_{nb}^p. Similarly, if the formation of a bubble nucleus was a slow event on the voltammetric timescale, one might expect an increase in the peak current at increasing scan rates.

The rate of critical bubble formation is a function of the activation energy (indicated in Fig. 1) by the Arrhenius equation $J = Z \exp(-E_a/kT)$. For homogeneous nucleation, J is a steep function of γ and supersaturation $(P_{gas} - P_{ambient})^7$
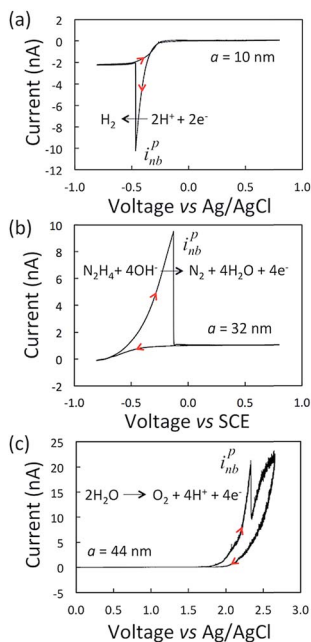

Fig. 2 Voltammograms corresponding to H_2, N_2, and O_2 bubble formation at Pt nano-electrodes. The gas-evolving electrode reactions are noted on the figure. The electrode radii, a, indicated on each plot were determined from the steady-state diffusion-limited current for ferrocene oxidation in acetonitrile. The aqueous solutions contained: (a) 0.5 M H_2SO_4, (b) 1 M N_2H_4, and (c) 0.25 M H_2SO_4.

$$J = Z \exp\left(\frac{-16\pi\gamma^3}{3kT\left(P_{\text{gas}} - P_{\text{ambient}}\right)^2}\right) \tag{3}$$

where J (m^{-3} s^{-1}) is the rate of critical bubble formation, the exponential pre-factor Z is treated as a constant, k is Boltzmann's constant, and T is temperature. For nucleation of bubbles from dissolved gas in solution, there is wide disagreement between experiment and theory, with nucleation often occurring at supersaturation levels that are orders of magnitude lower than predicted by eqn (3).[10,16–19] The literature presents a variety of explanations for the observed discrepancy, ranging from new thermodynamic interpretations of the surface tension of small nuclei,[6,20] to impinging cosmic rays,[21] to pre-existing stable nuclei.[16] Our current data does not allow speculation about nucleation rates aside from the observation that the rate appears to vary from extremely slow to very fast over a small voltage range ($\sim$5 mV), corresponding to a small change in the dissolved gas concentration.

A majority of the studies of nucleation in the literature similarly report a supersaturation value at which J becomes appreciably fast. There are three types of approaches that have been employed to measure the critical supersaturation at which bubble formation is observed: homogeneous gas-producing chemical reaction in bulk solution,[18,20,22,23] release of pressure after equilibrium is reached at elevated pressure[24,25] and electrochemical gas generation.[17,26] Lubetkin has compiled the results of a large number of these reports and points out that these measurements often reflect kinetic limitations and not true thermodynamic values.[27]

In the context of nucleation rates, i_{nb}^{p} represents a point in the J vs. supersaturation curve where bubble formation occurs quickly relative to the rate of change in gas supersaturation. For instance, at a 1 V s^{-1} scan rate, bubble nucleation reproducibly occurs within an $\sim$5 mV range. This voltage range, ΔV, is related to the characteristic time of the liquid-to-gas phase transition (τ) and the voltammetric scan rate, ν, by the relationship, $\tau = \Delta V/\nu$. In our experiments, at least one critical bubble forms at that dissolved gas supersaturation in the volume near the electrode at least every $\sim$5 ms, corresponding to a minimum nucleation frequency of 200 s^{-1}. Of course, the nucleation frequency may be much larger than this estimate of the minimum value.

Fig. 3 shows the dependence of i_{nb}^{p} for N$_2$ bubble formation on the radius of the Pt nanodisk, a. The upper part of the figure shows voltammograms recorded in aqueous 1 M N$_2$H$_4$ at Pt nanoelectrodes of 10, 23, 47, and 80 nm radius, and at a scan rate of 200 mV s^{-1}. It is apparent from these data that i_{nb}^{p} increases for N$_2$ bubble formation as a function of the electrode size; similar voltammetric behavior is observed from H$_2$ and O$_2$ bubble formation. The lower part of Fig. 3 shows that i_{nb}^{p} is a linear function of a for the nucleation of all three gases ($R^2 > 0.97$ in all cases). The solid lines in this plot represent least squares fits to the data that pass through the origin with slopes of 0.81 ± 0.02 nA nm^{-1}, 0.48 ± 0.03 nA nm^{-1} and 0.31 ± 0.01 nA nm^{-1} for H$_2$, O$_2$ and N$_2$, respectively.

The steady-state current at a nanodisk electrode, while typically written in terms of the bulk concentration of the reactants, can also be written as a function of the surface concentration of electrogenerated dissolved gas, C_{surf}. Assuming
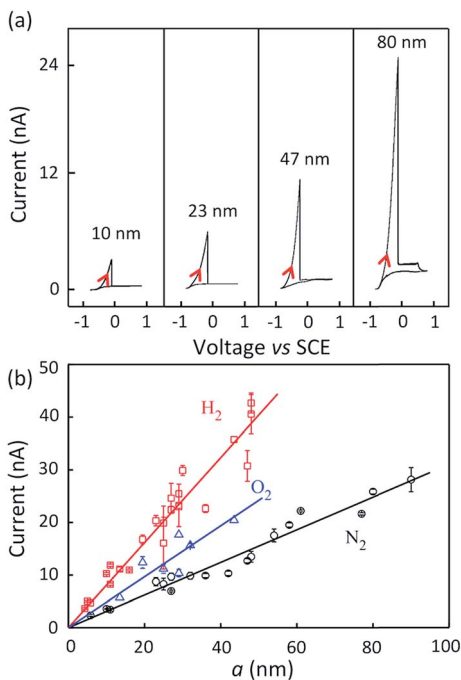
Fig. 3 Top: Voltammetry corresponding to the formation of stable N_2 bubbles at Pt nanoelectrodes of varying radii (labeled) in a 1 M N_2H_4 aqueous solution. Bottom: Plot of the i_{nb}^P as a function of the electrode radius, a, for H_2, N_2, and O_2. Similar data were originally presented in ref. 12–14.

zero concentration of the gas in bulk solution, the relation between current and C_{surf} is given by:[28]

$$i = 4naFDC_{surf} \qquad (4)$$

where D is the diffusion coefficient of the gas in solution and n the number of electrons transferred in the reaction ($n = 2$ for H_2, 4 for N_2, and 4 for O_2). Rearranging this equation, and setting i to i_{nb}^P allows one to obtain the critical concentration of dissolved gas at the electrode surface at the moment that a dynamically stable bubble is nucleated.

$$C_{crit} = i_{nb}^P/4naFD \qquad (5)$$

Because the plots of i_{nb}^P vs. a in Fig. 3 are linear, we conclude that C_{crit} is independent of the electrode size and can be calculated from eqn (5). Values of C_{crit} for H_2 (0.23 M), N_2 (0.09 M) and O_2 (0.14 M) are tabulated in Table 1, with errors determined from the variance in linear fits and uncertainty in the value of D (see Appendix C for details). The large supersaturation values associated with i_{nb}^P for each gas justify the use of eqn (4) and (5), which are based on the assumption that the bulk dissolved gas concentration is negligibly small.

A number of properties of the critical bubble nucleus, also listed in Table 1, are derivable from the values of C_{crit}. In computing these properties, we note that

Table 1 Parameters describing the critical nuclei for H_2, N_2, and O_2 bubble generation

	H_2		H_2 + surfactant		N_2		O_2	
	Ideal	Corrected	Ideal	Corrected	Ideal	Corrected	Ideal	Corrected
C_{crit} (M)	0.23 ± 0.02		0.14 ± 0.02		0.09 ± 0.02		0.14 ± 0.01	
ΔP_{Y-L} (atm)	290 ± 30[a]	350 ± 30[b]	180 ± 30	210 ± 30	140 ± 30	160 ± 40	100 ± 10	120 ± 10
r_{crit} (nm)	4.9 ± 0.6[c]	3.6 ± 0.3[d]	4.1 ± 0.8	3.5 ± 0.6[e]	10 ± 3	7.9 ± 1.6	14 ± 2	10 ± 1
n_{crit}[f]	3500 ± 900	1700 ± 300	1300 ± 500	900 ± 300	15 000 ± 9000	8100 ± 2500	28 000 ± 9000	12 000 ± 3000

[a] Pressure difference calculated directly from Henry's law at 25 °C and 1 atm in pure water ($\Delta P_{Y-L} = C_{crit}/K_H - 1$). [b] Pressure difference corrected using experimental gas solubility at high pressure in pure water and accounting for electrolyte reduction of solubility, see Appendix C, eqn (A6). [c] Calculated using the ideal ΔP_{Y-L} and surface tension of the air/solution interface at 1 atm. [d] Calculated using corrected ΔP_{Y-L} and modification of the interfacial tension by surface adsorption of gas at high pressures, see Appendix C. [e] Calculated using the surface tension of the air/solution interface at 1 atm, ΔP_{Y-L} and the ideal gas C. [f] Calculated from r_{crit}, ΔP_{Y-L} and the ideal gas law (eqn (7)) assuming a bubble of spherical geometry.

although the overall electrochemical system is not present in a true equilibrium state, local equilibrium is assumed to be maintained between the solution containing dissolved gas and the gas bubble. The Laplace pressure of a critical nucleus is directly related to C_{crit} by the partial pressure of the dissolved gas ($P_{gas} = \Delta P_{Y-L} + P_{ambient}$). This relationship is given in a rudimentary way using Henry's law ($K_H P_{gas} = C$), which upon substitution of $P_{gas} = \Delta P_{Y-L} + P_{ambient}$, and rearrangement, yields:

$$\Delta P_{Y-L} = (C_{crit}/K_H) - P_{ambient}. \tag{6}$$

K_H is equal to 0.78 mM atm^{-1} for H_2 in pure water at 25 °C.[29] Thus, for the measured $C_{crit} = 0.23$ M, eqn (6) yields $\Delta P_{Y-L} = 290$ atm. This Laplace pressure is a thermodynamic quantity, which is related through the surface tension, γ, to the bubble radius of curvature, i.e., the critical bubble radius, by eqn (2). Using the macroscopic surface tension of 0.5 M H_2SO_4 at ambient temperature and pressure (0.072 N m^{-1})[30] as a simple estimation of γ, we calculate the value of $r_{crit} = 4.9$ nm. From this we compute the number of molecules, n_{crit}, in the critical nucleus using the ideal gas law, assuming a spherical nucleus of volume $(4\pi/3)r_{crit}^3$.

$$n_{crit} = (\Delta P_{Y-L} + P_{ambient})4\pi r_{crit}^3/3RT \tag{7}$$

For the 4.9 nm radius critical H_2 nucleus, formed at 1 atm and 298 K, the total internal pressure is 291 atm, and the critical nucleus contains ∼3500 H_2 molecules.

The thermodynamic relations used above provide a straightforward means to estimate parameters describing the critical bubble nucleus and are listed as ideal values in Table 1. Better estimates of ΔP_{Y-L}, r_{crit}, and n_{crit} can be obtained by consideration of known non-idealities at high pressures. The corrected values in Table 1 are based on reported measurements of gas solubility in pure water at high pressure, the reduction of gas solubility by electrolyte at ambient pressures (i.e., 'salting out'), and reduction of surface tension by gas adsorption at high pressure. These corrections are detailed in Appendix C. Another consideration is that the surface tension is a function of the interfacial radius of curvature for very small bubbles.[31] The size at which the effect becomes important is highly debated. However, experimental studies of capillary condensation have shown the surface tension of water and cyclohexane droplets as small as ∼5 nm to be very nearly equal to the bulk value.[32,33] Thus, the possible dependence of γ on bubble radius is ignored here.

It is expected from classical nucleation theory that a solution/gas interface with lower surface tension will have a significantly lower value of ΔG_{surf} and hence a lower value of E_a for the spontaneous formation of a critical nucleus, Fig. 1. However, both Rubin et al.[18] and Hemmingsen[24] observed only marginally lower critical values for N_2 supersaturation induced by a chemical reaction, and for argon supersaturation induced by pressure release, respectively, in the presence of surfactant, and argued that the surfactant concentration in the bulk was too low to affect homogeneous nucleation. To test this idea, we investigated the effect of surfactant on the H_2 system. Fig. 4 demonstrates the influence of adding cetyltrimethylammonium bromide (CTAB) to the solution on the value of i_{nb}^p. The voltammograms show the formation of a H_2 bubble in 0.5 M H_2SO_4 in the
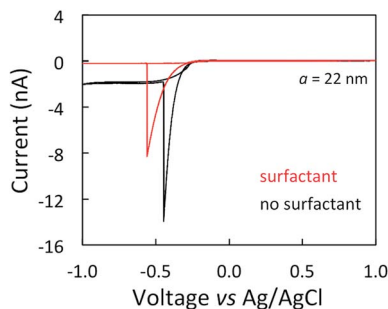
Fig. 4 $i-V$ responses from a 22 nm radius Pt electrode in 0.5 M H_2SO_4 with (red) and without 0.2 mg mL^{-1} CTAB surfactant (black). Scan rate 100 mV s^{-1}.

presence and absence of 0.2 mg mL^{-1} CTAB, recorded at the same 22 nm radius electrode. We observe a reduction of ~40% of i_{nb}^p in the presence of surfactant, which is reproducible with different electrodes, indicating that nucleation proceeds at a lower critical supersaturation of H_2. This finding indicates that a critical bubble nucleus in the presence of CTAB has a lower internal pressure, suggesting that the lifetime of a sub-critical radius nucleus, as it grows to critical size, is long enough for surfactant to adsorb to its surface. While both gas and surfactant adsorption reduce surface tension, it has been shown that the two components are not additive. Rather, the two components are in competition for available surface area.[34] Thus, for the CTAB data, in contrast to the other experiments, we do not account for gas adsorption in the corrected value of r_{crit} reported in Table 1.

Both ideal and corrected values of ΔP_{Y-L}, r_{crit}, and n_{crit} for O_2 and N_2 bubble nucleation were computed as above and are listed in Table 1. The supersaturation pressure values corresponding to a nucleation event range between 100 and 350 atm and are dependent upon gas type. These values are as large as the largest reported values listed by Lubetkin,[27] and the magnitude of supersaturation and ordering by gas type $O_2 < N_2$ (H_2 not studied) agree approximately with Hemmingsen,[24] who visually observed bubble formation after release of pressure to ambient conditions. In comparison to the decompression method, our results are significantly more precise and the electrochemical method is simpler. Our measured critical supersaturation values are an order of magnitude larger than other reports of electrochemically induced supersaturation. Dapkus and Sides[17] attributed the relative ease of nucleation in their electrochemical system to a reduction of surface tension by the large electric field within the double layer at the electrode surface. Here we do not speculate on electric field effects; however, in the following section, we do consider how bubble nucleation might be influenced by proximity to a gas-evolving surface.

The results presented in Table 1 indicate at least a few thousand molecules need to spontaneously assemble to form a critical bubble with r_{crit} between ~4 and ~10 nm. In the case of H_2, this process occurs at a C_{crit} of ~0.23 M. If we consider a homogeneous solution containing 0.23 M H_2, the requisite number of molecules to form a critical bubble ($n_{crit} = 1700$) is found within a spherical volume of solution having a radius of 14 nm. A bubble nucleus will deplete the

surrounding solution of dissolved gas as it grows, relying upon diffusion of individual H_2 molecules to the growing bubble. Random diffusion of thousands of molecules to a growing bubble within this volume is an unlikely event. However, in our experiment, the Pt nanoelectrodes can support an immense rate of H_2 generation due to the high catalytic rate for H^+ reduction at Pt, as well as the large convergent diffusional flux of H^+ to the nanoscale electrode. For instance, a typical 16 nA peak current at a 20 nm radius electrode is equivalent to the production of $\sim 10^{11}$ H_2 molecules per second, corresponding to the generation of the requisite $\sim 10^3$ molecules, in 3 nanoseconds, for a H_2 bubble of radius equal to r_{crit}. Thus a growing sub-critical bubble nucleus near the Pt nanoelectrode will not deplete the local concentration of dissolved gas, and its growth will thus not likely be transport limited.

We performed steady-state finite element simulations to gain further insight into the flux and concentration distributions of H_2 around a bubble nucleus at an electrode. Mass transport of H_2 in the solution and H_2 transfer exchange at the bubble–solution interface were modeled in these simulations (detailed description in Appendix B). The results are shown in Fig. 5 for three bubble nuclei of radii that are, respectively, smaller, larger and nearly equal to the value of $r_{crit} = 4.9$ nm reported in Table 1. In each simulation, the bubble is situated 1 nm above a 20 nm radius electrode that generates a uniform surface flux of H_2 equivalent to the current experimentally observed at i_{nb}^p (16.2 nA). The concentration of H_2 is represented by color (red = high concentration, blue = low concentration); its value at the surface of the bubble is fixed to that given by Henry's law and the bubble's internal pressure (eqn (6)). The streamlines represent H_2 flux, from which we observe that the H_2 generated at the electrode underneath the bubble diffuses into the bubble, whereas the H_2 generated at the electrode far from the bubble
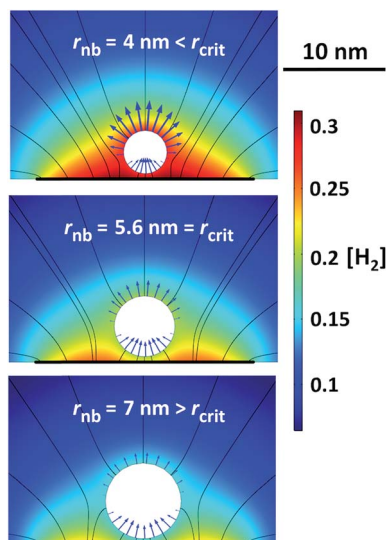

Fig. 5 Finite element simulations of 4, 5.6, and 7 nm-radius bubble nuclei positioned one nanometer above a 20 nm radius Pt electrode. Streamlines represent H_2 flow away from the electrode and vectors show the flux across the bubble surface.

diffuses into bulk solution. The arrows at the bubble–solution interface represent H_2 flux vectors across the interface; the results in Fig. 5 indicate that H_2 enters the bottom of the bubble that is close to the electrode surface, and exits through the top surface of the bubble. The magnitudes of these fluxes are quite different for the different sized nuclei. The smallest bubble nucleus ($r_{nb} = 4$ nm), which has the highest internal pressure, has a larger H_2 flux out of the top of the nucleus and a smaller flux into its lower side. Overall, this gives a net outward flow of H_2, and hence this sub-critical nucleus will tend to collapse. In contrast, for the largest bubble ($r_{nb} = 7$ nm), the lower internal pressure generates a lower surface concentration and the net flux of H_2 is into the bubble; *i.e.*, this is a growing bubble. The net inward flux (7.1 fmol s^{-1} integrated over the bubble surface) is such that enough gas enters the bubble to grow it to a hemisphere equal to the size of the electrode in ~7 μs. The 5.6 nm bubble corresponds to a size where the H_2 fluxes into and out of the bubble, through the lower and upper surfaces, are nearly perfectly balanced; however, any perturbation would cause the bubble to either grow or shrink. Note that this simulated bubble size is just slightly larger than $r_{crit} = 4.9$ nm reported in Table 1 for H_2.

For simplicity, the lower edge of the bubble nucleus in Fig. 5 was fixed 1 nm from the electrode center in the simulations; however, moving the nucleus horizontally or vertically only subtly affects the calculated values and not the qualitative conclusion that the proximity of the electrode provides a sufficient supply of the gas to support the rapid growth of the bubble. Moreover, simulations with the different gases show similar flux distributions, although the exact concentrations/ critical sizes depend on the gas. As the simulations were performed at steady state, they do not capture the time dependence; however, they do reflect the expected direction and magnitude of the local fluxes (NB: the use of steady-state simulations accounts for the anomalously high concentration observed around the 4 nm bubble, which, rather than constantly generating H_2 while maintaining its size, would actually be shrinking).

The primary conclusion we draw from the simulations is that the close proximity of the bubble nucleus to the electrode/electrolyte interface greatly reduces kinetic limitations to bubble growth that may result from improbable stochastic fluctuation in the dissolved gas concentration required to reach r_{crit}. However, we also note that the results of these simulations are semi-quantitatively consistent with the values of the critical nucleus size listed in Table 1. Specifically, the simulations indicate that bubbles with $r_{nb} < r_{crit}$ (~5 nm for H_2) will dissolve, while bubbles with $r_{nb} > r_{crit}$ will continue to grow. The apparent consistency of the simulated kinetic phenomena (*i.e.*, diffusion) with the conclusions based on thermodynamic relationships is highly satisfactory.

In the above discussions, we have considered homogeneous nucleation occurring in the solution. However, as suggested by the above simulations, nucleation might be a pseudo-homogeneous process in which bubble growth is a surface mediated process whereby the constituent gas is delivered over a short diffusive distance. Heterogeneous nucleation involving gas adsorption on the Pt surface is also a possible mechanism, in which a sphere cap nucleus is formed at the electrode surface. Our computed values of r_{crit}, which began with the experimentally measured C_{crit}, did not require knowledge of the bubble geometry, other than assuming a surface curvature that is spherical. Hence the critical radius for nucleation we calculate is independent of mechanism. However, for

heterogeneous nucleation, the bubble surface area and volume are defined by the contact angle of the sphere cap on the Pt surface. The C_{crit} for heterogeneous nucleation may be lower compared to homogeneous nucleation because fewer molecules are required for a smaller sphere cap shaped bubble on the electrode surface, and the energy cost for creating a smaller bubble surface is lower. If heterogeneous nucleation is occurring in our system, surface adsorption of the bubble nucleus to the electrode would likely need to be directed by hydrophobic surface contaminants. Surface roughness would also be variable from electrode to electrode and consequently the critical concentration, and thus values of observed values of i_{nb}^p, would be expected to be less reproducible using different electrodes than our results suggest. However, we cannot discount this possibility.

Conclusions

In this report, we have demonstrated that the study of single gas bubbles at Pt nanodisk electrodes allows precise quantitative evaluation of key parameters describing bubble nucleation. Specifically, analysis of the voltammetric peak currents at the instant preceding stable bubble formation provides the size, internal pressure, and number of gas molecules of the critical size nucleus that grows into a stable bubble. We find that the critical nuclei for H_2, O_2 and N_2 bubbles have a radius between 4 and 10 nm, an internal pressure of 100 to 350 atm, and contain between 2000 and 10 000 molecules, with the variation arising from a number of physicochemical parameters of the gas (*e.g.*, diffusion coefficient, gas solubility, surface tension, *etc.*). The origin of the largest uncertainty in these values arises from the uncertainty in the gas diffusivity in electrolyte solution, as well as potential unknown limitations of applying thermodynamic relationships at nanoscale length scales for single entities (*i.e.*, individual gas nanobubbles).

Our current investigations do not shed significant insight into the frequency of transient bubble formation and collapse prior to the formation of a nucleus with radius > r_{crit} that grows into a dynamically stable bubble. The voltammetric data place a lower bound of $\sim$200 s^{-1} for nuclei generation when the electrode is held at a potential in immediate vicinity of the nucleation potential. We are currently exploring measurements on single bubble experiments to estimate nucleation rates for gas bubbles, and these studies will be communicated in a future report.

Appendix A: experimental methods

Nanoelectrodes were fabricated as previously reported.[35] Briefly, the end of a 25 μm Pt wire was sharpened by etching in 6 M sodium cyanide, the wire attached to a tungsten rod, and the sharp end sealed in a glass capillary in a H_2/air flame. The glass was then polished on silicon carbide sandpaper (400/1200 grit Buehler) until a Pt nanodisk was exposed, as indicated by an electronic feedback circuit. The electrochemically-apparent electrode radius, a, was determined by measurement of the steady-state diffusion-limited current for ferrocene oxidation in an acetonitrile solution containing 0.1 M tetrabutylammonium hexafluorophosphate (TBAPF$_6$). Radii were calculated using[28]

$$i_{lim} = 4nFD_{Fc}C^*a$$

where n is the number of electrons transferred ($= 1$ for Fc), F is Faraday's constant ($= 96\,485$ C mol^{-1}), and D_{Fc} (2.5×10^5 cm^2 s^{-1})[36] and C^* are the diffusion coefficient and bulk concentration of ferrocene (5 mM), respectively.

Sulfuric acid, hydrazine, and CTAB (Sigma Aldrich) were used as received. Ferrocene was purified by sublimation. A Dagan Cornerstone Chem-Clamp and a Pine RDE4 (used as a waveform generator) were interfaced with a PCI data acquisition card (National Instruments) to perform the voltammetric experiments.

Appendix B: description of finite element simulations

The concentrations and fluxes of H_2 presented in Fig. 5 were calculated by numerically solving the equations describing H_2 diffusion and H_2 transfer at the bubble–solution interface. Boundary conditions were chosen to match those of experiments with a 20 nm radius electrode in 0.5 M H_2SO_4 at the experimentally determined i_{nb}^p ($=16.2$ nA) and for a range of bubble nuclei sizes. The lower edge of the bubble was placed 1 nm above the nanoelectrode center, as shown in Fig. 6.

Mass transfer was described by the steady-state diffusion equation (eqn (A1)) within the axially symmetric domain shown in Fig. 6.
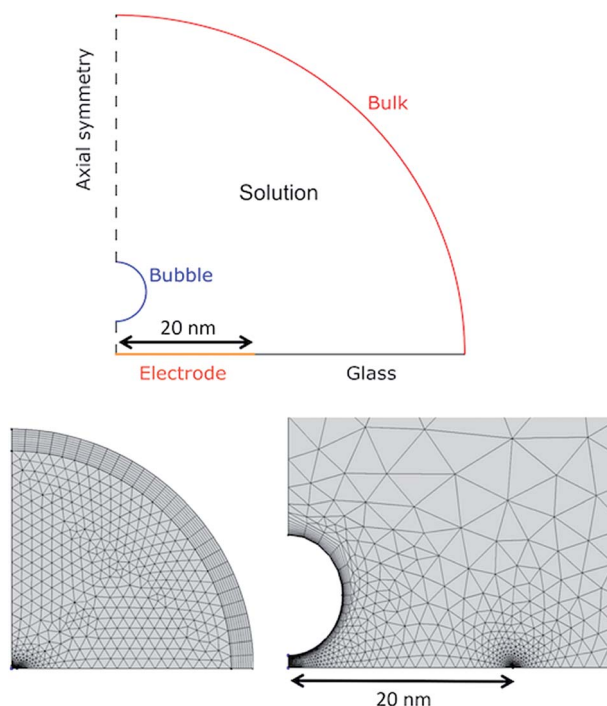
$$0 = D_{H_2}\nabla^2 c \tag{A1}$$

Fig. 6 Geometry (not to scale) and mesh for finite element simulations of a bubble nucleus above a nanoelectrode.

here, D_{H_2} ($=4.5 \times 10^{-5}$ cm^2 s^{-1}) and c are the diffusion coefficient and concentration of H_2, respectively. The concentration at the bulk boundary was taken to match that of the experimental conditions, that is

$$c_{H_2} = 0 \text{ M} \qquad \text{(A2)}$$

There is no flux of H_2 into, or out of, the glass surrounding the nanoelectrode, as described by

$$0 = D_{H_2} \nabla c \cdot \vec{n} \qquad \text{(A3)}$$

where $\vec{n}$ is the inward pointing unit normal to the surface.

On the surface of the bubble, we assume that the gas transfer kinetics are infinitely fast, *i.e.*, always at equilibrium. We use the Young–Laplace equation (eqn (6)) to describe the internal pressure and Henry's law to determine its equilibrium concentration. The bubble surface concentration of H_2 is thus described by:

$$C_{H_2} = k_H \left(P_{Ext} + \frac{2\gamma}{r_{nb}} \right). \qquad \text{(A4)}$$

The boundary condition on the electrode was matched to the experimentally determined current ($i_{nb}^p = 16.2$ nA, for $r_{elec} = 20$ nm) such that the H_2 flux is distributed evenly across the electrode surface, which is a reasonable assumption for a kinetically limited reaction, *i.e.* at moderate electrode overpotentials.

$$\frac{-i_{nb}^p}{2F\pi a^2} = D_{H_2} \nabla c \cdot \vec{n} \qquad \text{(A5)}$$

Solution of eqn (A1) was achieved using the commercial finite element package COMSOL Multiphysics (version 5.2). The mesh, which was heavily refined on the boundary between the glass and the Pt and the bubble surface, is shown in Fig. 6.

The "infinite elements" coordinate transform was used to map the outer region (quadrilateral mesh in Fig. 6) to infinity to rule out any influence of a finitely sized domain of simulation.

Appendix C: calculation of parameters for the critical nuclei in Table 1

Table 2 lists diffusion coefficients for H_2, N_2, and O_2 in water from different literature reports. In evaluation of C_{crit} from the i_{nb}^p *vs.* a slopes in Fig. 3, the diffusion coefficients for each gas were averaged and the extrema were used to estimate the uncertainty in D.

The ideal values in Table 1 in the main text are calculated using straightforward classical thermodynamic relationships (see main text). Henry's law is the most well studied reference point for gas solubility. At 25 °C and 1 atm, K_H is 0.78, 0.69, and 1.39 mM for H_2, N_2, and O_2 in pure water, respectively.[29,40,41] However, calculation of the values using Henry's law implicitly assumes that gas solubility increases linearly with increasing pressure. Empirical measurements of gas

Table 2 List of diffusion coefficients found in the literature for each gas type

	H_2	N_2	O_2
Diffusivity (10^{-5} cm^2 s^{-1}) at 25 °C (ref. 37)	4.50	1.88	2.10
Diffusivity (10^{-5} cm^2 s^{-1}) at 20 °C (ref. 38)	4.25	2.00	2.30
Diffusivity (10^{-5} cm^2 s^{-1}) at 20 °C (ref. 39)	5.0	2.6	2.3
Average ± extremum (10^{-5} cm^2 s^{-1})	4.58 ± 0.33	2.16 ± 0.44	2.23 ± 0.13

solubility in pure water at extreme pressures are available in the literature and report significant deviation from the linear approximation.[29,42,43] Fig. 7 compares the linear approximation with the empirical data. The pressure at which the equilibrium solubility matches our measured C_{crit} is a more accurate partial pressure, which we denote by $P_{gas}(C_{crit})$.

From the data presented in Fig. 7 we obtain the pressure in equilibrium with the critical concentration for H_2 ($C_{crit} = 0.23$ M), as $P_{gas}(C_{crit}) = 310$ atm, slightly larger than the ideal value, 290 atm, calculated with the Henry's law (linear) approximation. An additional correction concerns the electrolyte's effect on dissolved gas solubility ("salting out"). As no measurements of this effect are available at high pressure, we assume that the fractional change is the same at all pressures. Thus, this is included through multiplying $P_{gas}(C_{crit})$ by the ratio of equilibrium solubility at 1 atm in pure water and with electrolyte present. The corrected value for ΔP_{Y-L}, which is reported in Table 1 as 'corrected' is given by

$$\Delta P_{Y-L} = P_{gas}(C_{crit})K_H(\text{water})/K_H(\text{electrolyte}) - P_{ambient} \quad \text{(A6)}$$

For instance, the Henry's law constant for H_2 in 0.5 M H_2SO_4 is 89% of the value in pure water (both at 1 atm);[44] consequently, our measured C_{crit} represents a higher ΔP_{Y-L} of 350 atm. Experimental studies of gas solubility in the electrolyte solutions employed in this study would allow us to further refine these approximations.

Additionally, it is not expected that the surface tension of a bubble nucleus is equal to that of the air/solution interface at atmospheric pressure. At high
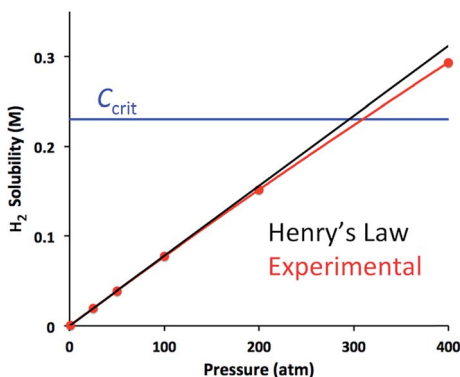

Fig. 7 Plot of experimental values (red) of H_2 solubility at high pressures from Wiebe *et al.*[29] Compared with Henry's law linear approximation.

pressures, gases are known to adsorb to the gas/solution interface, reducing the surface tension to different extents according to their polarizability. Depending on the gas and the pressure within the critical nucleus, the reduction in surface tension can be significant and would proportionally lower the estimated r_{crit}. For the gases in this study, the order of increasing positive gas adsorption to the interface has been empirically measured as $H_2 < O_2 < N_2$.[45] Measurements of the surface tension of gas/water interfaces were reported up to 80 atm. Polynomial fits to the data are provided in the form $\gamma = \gamma_0 + BP + CP^2$ where γ_0 (dyn cm^{-1}) is the surface tension at 1 atm, P is the applied pressure, and B and C are the fit parameters. Values for B and C were reported as -0.0250 and 0, -0.0835 and 0.000194, and -0.0779 and 0.000104 for H_2, N_2, and O_2, respectively. Values of 72 and 73 dyn cm^{-1} were used for γ_0 for the H_2SO_4 and N_2H_4 solutions, respectively,[30,46] giving corrected values for γ of 63, 65, and 64 dyn cm^{-1} for H_2, N_2, and O_2, respectively. Note, as stated in the main text, as the influence of the surfactant (CTAB) cannot easily be combined with that of the gas altering the surface tension, we used the surface tension at 1 atm in all cases ($\gamma = 37$ dyn cm^{-1}).[47] From these surface tensions and the corrected pressure we derived the corrected values of r_{crit} displayed in Table 1, from which the number of molecules in the critical nucleus, n_{crit}, were deduced using the ideal gas law (eqn (7), with the corrected pressure).

Conflict of interest

The authors declare the following competing financial interest: Sean German is an employee of Revalesio Corporation.

Acknowledgements

References

1 M. Volmer and A. Weber, *Z. Phys. Chem.*, 1926, **119**, 277.

2 R. Becker and W. Doring, *Ann. Phys.*, 1935, **24**, 719.

3 J. Frenkel, *Kinetic Theory of Liquids*, Dover, New York, 1955.

4 Y. B. Zeldovich, *Acta Physicochim. URSS*, 1943, **18**, 1.

5 M. S. Plesset and A. Prosperetti, *Annu. Rev. Fluid Mech.*, 1977, **9**, 145.

6 V. K. Shen and P. G. Debenedetti, *J. Chem. Phys.*, 2003, **118**, 768.

7 V. Talanquer and D. W. Oxtoby, *J. Chem. Phys.*, 1995, **102**, 2156.

8 S. Goldman, *J. Phys. Chem. B*, 2008, **112**, 16701.

9 M. Blander and J. L. Katz, *AIChE J.*, 1975, **21**, 833.

10 C. Ward, A. Balakrishnan and F. C. Hooper, *Trans. ASME*, 1970, **92**, 695.

11 L. Luo and H. S. White, *Langmuir*, 2013, **29**, 11169.

12 Q. Chen, L. Luo, H. Faraji, S. W. Feldberg and H. S. White, *J. Phys. Chem. Lett.*, 2014, **5**, 3539.

13 Q. Chen, H. S. Wiedenroth, S. R. German and H. S. White, *J. Am. Chem. Soc.*, 2015, **137**, 12064.

14 Q. Chen, L. Luo and H. S. White, *Langmuir*, 2015, **31**, 4573.

15 S. R. German, Q. Chen, M. A. Edwards and H. S. White, *J. Electrochem. Soc.*, 2016, **163**, 3160.

16 E. N. Harvey, D. K. Barnes, W. D. McElroy, A. H. Whiteley and D. C. Pease, *J. Am. Chem. Soc.*, 1945, **67**, 156.

17 K. V. Dapkus and P. J. Sides, *J. Colloid Interface Sci.*, 1986, **111**, 133.

18 M. B. Rubin and R. M. Noyes, *J. Phys. Chem.*, 1992, **96**, 993.

19 P. M. Wilt, *J. Colloid Interface Sci.*, 1986, **112**, 530.

20 P. G. Bowers, K. Bar-Eli and R. M. Noyes, *J. Chem. Soc., Faraday Trans.*, 1996, **92**, 2843.

21 D. Sette and F. Wanderlingh, *Phys. Rev.*, 1962, **125**, 409.

22 Y. Mori, K. Hijikata and T. Nagatani, *Int. J. Heat Mass Transfer*, 1976, **19**, 1153.

23 M. J. Hey, A. M. Hilton and R. D. Bee, *Food Chem.*, 1994, **51**, 349.

24 E. A. Hemmingsen, *J. Appl. Phys.*, 1975, **46**, 213.

25 S. Jones, G. Evans and K. Galvin, *Adv. Colloid Interface Sci.*, 1999, **80**, 27.

26 D. E. Westerheide and J. W. Westwater, *AIChE J.*, 1961, **7**, 357.

27 S. Lubetkin, *Langmuir*, 2003, **19**, 2575.

28 A. J. Bard and L. R. Faulkner *Electrochemical Methods: Fundamentals and Applications*, John Wiley and Sons, New York, 2001.

29 R. Wiebe, V. L. Gaddy and C. Heins Jr, *Ind. Eng. Chem.*, 1932, **24**, 823.

30 R. M. Suggitt, P. M. Aziz and F. Wetmore, *J. Am. Chem. Soc.*, 1949, **71**, 676.

31 R. C. Tolman, *J. Chem. Phys.*, 1949, **17**, 333.

32 M. M. Kohonen and H. K. Christenson, *Langmuir*, 2000, **16**, 7285.

33 L. R. Fisher and J. N. Israelachvili, *Nature*, 1979, **277**, 548.

34 C. Jho and A. D. King Jr., *J. Colloid Interface Sci.*, 1979, **69**, 529.

35 B. Zhang, J. Galusha, P. G. Shiozawa, G. Wang, A. J. Bergren, R. M. Jones, R. J. White, E. N. Ervin, C. C. Cauley and H. S. White, *Anal. Chem.*, 2007, **79**, 4778.

36 T. Kuwana, D. E. Bublitz and G. Hoh, *J. Am. Chem. Soc.*, 1960, **82**, 5811.

37 E. L. Cussler, *Diffusion: Mass Transfer in Fluid Systems*, Cambridge University Press, New York, 1997.

38 P. T. H. M. Verhallen, L. J. P. Oomen, A. J. J. M. v. d. Elsen and J. Kruger, *Chem. Eng. Sci.*, 1984, **39**, 1535.

39 D. L. Wise and G. Houghton, *Chem. Eng. Sci.*, 1966, **21**, 999.

40 R. Battino, T. R. Rettich and T. Tominaga, *J. Phys. Chem. Ref. Data*, 1983, **12**, 163.

41 R. Battino, T. R. Rettich and T. Tominaga, *J. Phys. Chem. Ref. Data*, 1984, **13**, 563.

42 V. I. Baranenko, V. S. Sysoev, L. N. Falkovskii, V. S. Kirov, I. Piontkovskii and A. N. Musienko, *At. Energy*, 1990, **68**, 162.

43 M. Geng and Z. Duan, *Geochim. Cosmochim. Acta*, 2010, **74**, 5631.

44 P. Ruetschi and R. F. Amlie, *J. Phys. Chem.*, 1966, **70**, 718.

45 R. Massoudi and A. D. King Jr, *J. Phys. Chem.*, 1974, **78**, 2262.

46 N. B. Baker and E. C. Gilbert, *J. Am. Chem. Soc.*, 1940, **62**, 2479.

47 Z. Adamczyk, G. Para and P. Warszynski, *Langmuir*, 1999, **15**, 8383.